Wave evolution across the Louisiana shelf

Anita Engelstad[a], T. T. Janssen[a,b], T. H. C. Herbers[c], Gerbrant van Vledder[d], Steve Elgar[e], Britt Raubenheimer[e], Lincoln Trainor[f], Ana Garcia-Garcia[g]

[a] Department of Geosciences, San Francisco State University, San Francisco, CA 94132, USA

[b] Theiss Research, San Diego, La Jolla, CA 92037, USA

[c] Department of Oceanography, Naval Postgraduate School, Monterey, CA 93943, USA

[d] Environmental Fluid Mechanics Section, Civil Engineering and Geosciences, Delft University of Technology, 2600 GA, Delft, The Netherlands

[e] Woods Hole Oceanographic Institution, Woods Hole, MA 02543, USA

[f] Royal Australian Navy, Australia

[g] Department of Earth and Planetary Sciences, University of California Santa Cruz, Santa Cruz, CA 95064, USA

Abstract

Observations and third-generation wave model hindcasts of ocean surface gravity waves propagating across the Louisiana shelf show that the effects of the mud environment on wave evolution are complex and episodic. Whereas low-frequency waves (0.04-0.20 Hz) show a consistent decay similar to earlier studies, the presence of

mud also appears to suppress the development of short waves (0.20-0.25 Hz) under fetch-limited growth conditions. Significant suppression of wave development under wind-forced conditions is found to occur almost exclusively during easterly winds when satellite images show the Atchafalaya mud plume extends into the study area. These results suggest that episodic sediment suspension events with high mud concentrations in the upper water column can affect the evolution of wind waves.

1 Introduction

The propagation and transformation of ocean surface waves in coastal areas is affected by many processes, including refraction, dissipation, and wind forcing, and is important for nearshore circulation, mixing, and transport processes. The presence of extensive muddy areas on the shelf and in the nearshore is known to strongly affect coastal wave transformation. However, the physical processes involved in the interaction between waves and mud, and the quantitative effects on the nearshore wave energy balance, are not fully understood.

Idealized models have been derived based on a discrete two-layer description of the water column, where surface waves drive internal waves on the density interface (lutocline) between the nearly inviscid water and a dissipative, muddy bottom layer (Gade, 1958; Dalrymple & Liu, 1978; Ng, 2000, Winterwerp et al. 2007, MacPherson, 1980; Piedra-Cueva, 1993; Mei & Liu, 1987) through direct interaction of the wave-induced near-bed fluid motions with the mud. However, field observations show that short waves, which do not interact strongly with the seafloor, also lose energy while traversing muddy areas (Sheremet and Stone, 2003; Sheremet et. al, 2005; Elgar and

Raubenheimer, 2008; Sheremet et. al, 2011), and that generation of high-frequency waves by wind during fetch-limited conditions can be suppressed (Trainor 2009). Such observations suggest that new processes should be considered in addition to direct wave-seafloor interaction.

The objectives of the present work are to improve understanding of how mud affects the nearshore wave energy balance for both longer swell waves and short, wind-driven seas, and the implications for coastal wave modeling. Here, recent observations of wave evolution across the inner Louisiana shelf, collected over two months during spring 2008 are presented. The experimental area is in the vicinity of the Atchafalaya outflow (figure 1a), and is characterized by extensive mud deposits on the seafloor and highly variable wave and wind conditions (section 2). To identify the effects of mud on the wave energy balance, the observations are compared with hindcast results from a third-generation wave model (section 3), and satellite observations of sediment plumes are used to investigate causes of model-data discrepancies during wind-forced conditions (section 4).

2 Field Observations

2.1 Field site

Wave evolution on the Louisiana shelf is complex and shaped by the semi-enclosed geometry of the Gulf of Mexico, which is decoupled from the Atlantic Ocean, and the presence of a relatively wide, shallow shelf. Meteorological forcing usually is weak from May through September, except for the passage of an occasional Hurricane in

late summer-early fall. From October through April, cold fronts pass through the area every three to seven days, resulting in locally generated wind seas with a wide range of wave heights and directions, and associated wind-induced sea level variations and coastal circulation patterns (Roberts et al., 1989; Moeller et al., 1993). Although these cold fronts can differ in intensity and duration, they typically cause a clockwise rotation of the wind from a southerly direction during the pre-frontal stage to a northerly direction during the post-frontal stage. High wind speeds and relatively longer fetches (southerly winds are approximately onshore, figure 1) during the pre-frontal phase often generate the most energetic wave fields.

Sediment discharge from the Atchafalaya River is carried along the coast in the primarily westward-directed Atchafalaya mud stream (Wells and Kemp, 1981). Sediment deposition extends to about 92.55° W (Draut et al., 2005) and is restricted to approximately shoreward of the 10 m isobath (Allison et al., 2000). The presence of mud on the Louisiana shelf is known to dampen wave energy near the coast (Sheremet and Stone, 2003; Sheremet et al. 2005; Kineke et al., 2006; Elgar and Raubenheimer, 2008; Trainor, 2009, Sheremet et al. 2011), and has been linked to the progradation of the eastern Chenier Plain (figure 1a) along a coast where most of the shoreline is retreating (Wells and Kemp, 1981; Roberts et al., 1989; Draut et al., 2005a).

2.2 Instrumentation

Instruments (figure 1b) deployed on the inner shelf from February 8 through March 29, 2008 included two directional wave buoys sampling continuously at 1.28 Hz, six bottom-mounted acoustic Doppler velocimeters (ADV) equipped with a built-in pressure gauge (sampling 68-minute bursts at 2 Hz every four hours), and five stand-

alone bottom-mounted pressure recorders sampling continuously at 2 Hz (figure 1b). An acoustic Doppler current profiler (ADP) was mounted on each of the ADV bottom frames as a back-up instrument, sampling 34-minute wave bursts at 1 Hz every hour. The instruments were arranged in two cross-shore arrays (hereafter referred to as the western and central transects, figure 1b) and an alongshore array (eastern transect; see also table 1, and Trainor, 2009; Engelstad, 2011). The western and central instrument transects were deployed in water depths ranging from 13 to 5 m, in a region with shore-parallel isobaths (figure 1b) on a fairly flat [bottom slope O(1:1000)] shelf. The eastern instrument array was located approximately 25 km off the coast and extended onto the Trinity Shoal in water depths from 11 to 5.5 m. Bottom-mounted instruments were recovered on March 2, 2008 (to check instrument operation, replace batteries, and retrieve the data), and redeployed on March 5, 2008. Time series lengths for all instruments (apart from the ADPs) were processed to fit the ADVs sampling length (68 minute duration time series every four hours). During the first deployment period, pressure-velocity data from the ADV at station pv4 produced noisy data and were replaced by data collected by the colocated ADP.

The nearshore instrument array (figure 1b) consisted of 10 bottom-mounted ADV-pressure sensor pairs along a cross-shore transect between 5- and 2-m water depths, deployed from February 14 to April 17, 2008. Time series were collected in 51-minute bursts at 2 Hz every two hours. The nearshore array connected to the western inner shelf array so that the combined dataset includes a 13 km-long, instrumented cross-shore transect from 13- to 2-m water depth. Wind speed and direction (figure 2a and 2b) were measured with a meteorological buoy located along the western transect (figure 1b). Box

core samples, taken in February 2008, identified a soft mud layer of less than 5 cm at each site at the time of sampling (Trainor, 2009; Garcia-Garcia et al., 2011). Although no instrument burial was observed, given the highly dynamic sediment transport in the area (± 10 cm bed level changes were observed at the nearshore array), it is possible that some changes in the surface mud layer thickness and rheology could have occurred over the course of the experiment.

To prevent errors due to the depth-attenuation of wave-induced pressure and velocity signals, and for consistency across different instruments, a cut-off frequency of 0.25 Hz was applied to all observations. The data were subdivided into low- (0.04-0.20 Hz) and high- (0.20-0.25 Hz) frequency bands. Wave heights were derived from the wave spectrum between 0.04 Hz and 0.25 Hz.

2.3 Wave conditions

A wide range of wind and wave conditions were observed associated with the passing of several cold fronts through the area (figure 2). The observed wave fields were dominated by locally generated wind seas with periods ranging from 4 to 8 s (figure 2c) and moderate wave heights (figure 2d), rarely exceeding 2 m.

During fetch-limited conditions (wind coming from northerly directions), observed wave heights at similar depths vary between the western and the eastern transect by as much as 60 percent, with wave heights largest in the east during northwesterly winds and larger in the west during northeasterly winds. For instance, on February 16, March 9 to 10, and March 16 to 17, during periods with strong northeasterly winds (these events are shaded in yellow in figure 2a and 2b), wave heights on the western transect are largest (compare the wave heights shaded in yellow in 11.3 m depth

in figure 3a with those in 10.9 m depth in figure 3b,c). Alternatively, on February 27 and March 8, during winds from the northwest (shaded in grey in figure 2a and b), waves are largest along the eastern transect (compare wave heights shaded in grey in 11.3 m depth in figure 3a with those in 10.9 m depth in figure 3b,c). These differences may be caused by large variations in effective fetch associated with the proximity of the coastline just north of the western and central transects, and the extreme shallow depths northeast of the eastern transect. In any case, it suggests that locally generated waves, and fetch-limited wave growth conditions, often are important in this area.

Spatial variations in wave height also are observed on March 18 to 19 (figure 3, shaded in blue) when winds are from the south and wave periods are relatively long (figure 2, shaded in blue). The decrease in wave height during this period of longer-period (swell-like) waves is especially strong on the (alongshore) eastern transect in water depths between 10.9 m and 5.5 m (shaded in blue in figure 3c) and depths between 3.9 m and 1.7 m on the western transect (shaded in blue in figure 3a). The spatial variations of longer-period wave heights differ from those for wind-sea dominated conditions on March 16 to 17, when strong winds are from the northeast (shaded in yellow in figure 2b and 2c). During the March 16-17 event (shaded in yellow in figure 3), wave heights on the eastern transect are fairly homogeneous (no along-array variations), whereas wave heights along the western transect vary considerably, suggesting that local variations in the wave field on the Louisiana shelf are considerably different during fetch-limited generation events than during depth-controlled swell events.

The bathymetry surrounding the western transect is nearly alongshore uniform. Therefore, the observed decrease in wave height for waves entering the region from

southerly directions (compare February 29, March 18 to 19, and March 26 in figure 3a, b with those dates in figure 2b) suggests that wave energy is lost during onshore propagation (further analyzed below). The loss in wave energy could be caused by bottom friction, wave breaking, or the interaction between waves and the seafloor mud layer in this area (Sheremet and Stone, 2003; Sheremet et al. 2005; Elgar and Raubenheimer, 2008; Trainor, 2009; Sheremet et al. 2011). It is known that dissipation can be enhanced in muddy regions through wave-mud interaction (Gade, 1958; Dalrymple & Liu, 1978; Ng, 2000; Sheremet and Stone, 2003; Sheremet et al. 2005; Elgar and Raubenheimer, 2008; Trainor, 2009; Sheremet et al. 2011), but it is difficult to separate the effects of seafloor rheology from other processes affecting the wave evolution, in particular because little is known about the mutual interaction between waves, currents, and mud, and the corresponding effects on wave damping across the shelf.

3 Analysis

To isolate changes in the wave field associated with the presence of the mud on the seafloor, the observed wave evolution is compared with hindcasts performed with a third-generation wave model (SWAN, Booij et al. 1999). The wave model (SWAN) was applied in non-stationary mode (see Appendix for details) using observed winds, water levels, currents, and wave conditions (boundaries), and run with a standard JONSWAP bottom friction term (Hasselmann et al., 1973) without additional physics to account for the interaction with a mud layer. The objective was to apply the model to represent wave evolution over an equivalent sandy shelf with the same geometry, and for the same

conditions as present during the experiment, so that systematic effects of the mud on the wave evolution can be distinguished from the interaction of waves with a sandy bottom (bottom friction), other sources of dissipation such as wave breaking and white-capping, and processes such as wind generation, nonlinearity, refraction and shoaling.

3.1 Wave heights

The model hindcasts are in fairly good agreement with the observed wave height variability during the experiment for all stations (figure 4). However, for fetch-limited conditions (northerly winds), the model tends to overestimate wave heights (figure 5b), whereas during onshore wave propagation (southerly winds), the agreement is considerably better (figure 5a).

The overestimation of wave heights during fetch-limited conditions is most noticeable at the more seaward sensors (h >= 8 m, figure 4a and 4b, e.g. February 26, March 23). Comparison of observed with modeled spectra during fetch-limited conditions (figure 6) shows that wave energy input above the peak frequency is greatly over-estimated in the model, which results in the observed overestimation of wave heights at the seaward stations. It appears that during slanting fetch and fetch-limited conditions, wind wave generation is hindered or suppressed (figure 6) when compared with the model-predicted evolution (see also Trainor, 2009). This model-data discrepancy could be caused either by enhanced dissipation on the inner shelf (not accounted for in the model), or by suppression of wind-wave generation in this area, both associated with the presence of mud on the seafloor and in the water column. Some of these differences also could be caused by model errors in the representation of shallow water, fetch-limited wave growth conditions (Ardhuin et al., 2007).

During other times, for instance on March 10 and March 26, observed and modeled wave heights agree at the most seaward stations (h >= 8 m, figure 4a and 4b), but wave heights are systematically over-predicted near the shore (h <= 4 m, figure 4c and 4d). The same trend is observed during relatively weak wind forcing, suggesting that observed bottom-induced dissipation is stronger than predicted by the model, consistent with observations from previous studies (Sheremet and Stone, 2003; Sheremet et al. 2005; Elgar and Raubenheimer, 2008; Trainor, 2009, Sheremet et al. 2011).

3.2 Local energy balance

Differences between observed and modeled wave height values are the result of the accumulation of differences in the energy balance along the propagation path of waves over the inner shelf, and are not readily related to local differences in the energy balance. To identify such local differences, consider the one-dimensional energy balance assuming stationary conditions

$$\frac{dF}{dx} = S, \qquad (1)$$

where S represents the sum of the source terms for dissipation, nonlinearity, and generation, and the cross-shore wave energy flux, F, is defined as

$$F = \rho g E c_g \cos\theta . \qquad (2)$$

Here, ρ and g are (constant) density and gravitational acceleration, E is the variance density, c_g is group speed, and θ is the mean wave angle of incidence at each frequency (measured positive counterclockwise from shore-normal, which is set at 10° from true North). The energy flux gradient, $\frac{dF}{dx}$, is estimated through finite differencing over

adjacent stations (for both the model hindcasts and the observations). The use of the one-dimensional energy balance (equation (1)) is reasonable because the bathymetry near the western and central transect is alongshore uniform and gradients in the alongshore direction can be neglected.

Overall, the hindcast predictions of the magnitude and the spectral distribution of the flux gradients agree reasonably well with the observations (compare figure 7a with figure 7b and compare figure 7d with figure 7e), both offshore ($h > 8$ m) and nearshore ($h < 4$ m). The events characterized by large, negative flux gradients are associated with strong dissipation (mostly in the low-frequency band (0.04-0.20 Hz), and occur during times of high wave energy.

Differences between model and observations are greatest at higher frequencies ($\geq$ 0.2 Hz), especially at the seaward stations (compare figure 7a with 7b), where the model does not reproduce the observed dissipation. In contrast with the observations that show either no growth (e.g. February 18, March 24 in figure 7a) or dissipation (around March 17 in figure 7a), the model predicts a number of wave growth events (positive energy flux gradients in figure 7b) where wind input dominates over dissipation.

Closer to shore, where dissipation rates usually are larger (and thus dominate over possible local generation), the model-data agreement in the spectral distribution is generally better (compare figure 7d with 7e).

The differences between the modeled and observed energy flux gradients suggest that dissipation in the low-frequency band (mostly owing to wave-bottom interaction) at this field site is somewhat higher than on an equivalent sandy shelf (see e.g. February 17, March 1, March 17, compare figure 7a with 7b), consistent with previous findings of

wave-mud damping in the region (Sheremet and Stone, 2003; Sheremet et al. 2005; Kineke et al., 2006; Elgar and Raubenheimer, 2008; Trainor, 2009; Sheremet et al. 2011). However, the observed spectral distribution of the dissipation associated with wave-bottom interaction agrees fairly well with the modeled dissipation (JONSWAP bottom friction), suggesting that the spectral signature of dissipation (and its dependency on relative depth) is similar.

However, an important difference between model and data is the observed dissipation (or lack of growth) at higher frequencies ($\geq$ 0.2 Hz) at the deeper instrument sites whereas the model predicts generation (figure 7a and 7b). To investigate these model-data differences for a range of wind and wave conditions, but without the dependency on the energy in the wave field, consider the normalized flux gradient, or growth rate, κ, defined as

$$\kappa = \frac{dF}{dx}\frac{1}{\overline{F}} \qquad (3),$$

where $\overline{F} = \rho g E c_g$ is averaged between adjacent stations over which the flux gradient is estimated.

The events during which modeled growth rates of the higher-frequency components greatly exceed observed growth rates (figure 8b, data in upper left quadrant) occur almost exclusively during easterly winds, suggesting that the model-data discrepancies are related either to the specific fetch geometry or to other physical parameters associated with the wind direction (and changes therein). There appear two exceptions (figure 8b, black triangles in the upper left quadrant), during which time the wind was not from the east, but dissipation is strong (model overpredicts wave growth).

However, note that during these times (see March 11 in figure 9), although the wind has turned, the current is still from the east (discussed more in section 4.2).

In contrast, the observed enhanced (relative to the model) dissipation at low frequencies (< 0.2 Hz) shows no correlation with wind direction (figure 8a, data left of the dashed line in the lower left quadrant), consistent with a bottom-induced damping effect that does not depend strongly on either the wind or wave direction. Thus, the model-data comparisons suggest that the processes affecting the dissipation in the low-frequency band are different than those in the high-frequency band. Moreover, whereas the observed enhanced damping of longer waves could be consistent with existing theory based on direct interaction of surface waves with the lutocline (the density interface), it remains unclear why the differences between observed and modeled wave growth show a strong dependency on wind direction.

Part of the systematic differences for fetch-limited growth during easterly winds may be owing to model shortcomings in the representation of slanting fetch wave growth conditions (Ardhuin et al., 2007). However, these observations do not show the frequency-dependent shift in wave directions that is characteristic of slanting fetch wave growth conditions (Ardhuin et al., 2007). Moreover, during fetch-limited conditions with winds from the northwest and north, the model predictions are generally in good agreement with the observations (February 18, March 19 in figure 9). It is mostly during easterly winds that large differences in the growth rates are seen (dissipation instead of growth, March 16-17 in figure 9), and as soon as the wind turns to west (through south) the model predictions agree well with the observations (March 19 in figure 9).

Another source of modeling errors of wave growth could be the interaction with longer waves (swell). However, during many of the cases where there are large differences in growth rates between model and observations (February 16, March 10, March 17 in figure 9), low-frequency energy levels were low (figure 7c). In contrast, during other times when low-frequency energy levels are elevated (March 7, March 20 in figure 9), observed and modeled wave growth are in good agreement (figure 9). The model-data comparisons suggest that the observed dependency on wind directions most likely is associated with the wave-mud dynamics (and changes therein), and not the result of model shortcomings under fetch-limited conditions.

4 Discussion

4.1 Wave-mud interaction

Despite its importance, the characteristics and physical mechanisms of the interaction between surface waves and a muddy seafloor are not understood well. Models have been derived based on a two-layer approach, where surface waves drive internal waves on the density interface (lutocline) between the nearly inviscid water overlying a dissipative, muddy bottom layer (Gade, 1958; Dalrymple & Liu, 1978; Ng, 2000). These models require a direct interaction of the wave-induced fluid motion with the mud layer (and therefore the seafloor) and could explain the observed enhanced dissipation at lower frequencies (< 0.2 Hz)

However, consistent with previous results (Sheremet and Stone, 2003; Elgar and Raubenheimer, 2008; Trainor, 2009; Sheremet et al. 2011), the results here show that

relatively short waves, which do not interact strongly with the seafloor, also lose energy while traversing muddy areas (or their growth appears suppressed in some cases). The losses at higher frequencies could be associated with near-resonant triad interactions that exchange energy among different frequency components of the wave field, and in particular can transfer energy to lower-frequency waves where it is dissipated (Sheremet et al. 2005; Elgar and Raubenheimer, 2008; Sheremet et al. 2011). However, it is unlikely that this process is dominant at the deeper stations considered here ($h > 8$ m) where triad interactions are weak (off-resonant), and thus transfer of energy to longer waves and subsequent dissipation would be far too slow to explain the observed differences between model and observations. Moreover, the observation that high-frequency suppression events occur almost exclusively during easterly winds is inconsistent with nonlinear energy transfers, which do not depend strongly on the direction of the wind.

Although relatively short waves can undergo weak bottom interactions and loose energy through a direct interaction with the seafloor, this process cannot explain the observed dependence on the wind direction. Thus, the comparisons with observations presented here suggest that existing models for wave mud interaction cannot completely explain the observed dissipation of the high-frequency components of the wave field during fetch-limited wave growth conditions.

4.2 Sediment plume extent

Although direct interaction of waves and mud, as well as nonlinear wave-wave interactions are important to wave propagation, they do not appear to explain the observed dissipation of high frequency short waves. Another potential source of variations in wave-mud interaction and wave dissipation is changing sediment

concentrations near the Louisiana coast. These concentrations fluctuate in response to changes in sediment discharge from the Atchafalaya River and adjacent waterways, as well as local resuspension of sediment by strong wave and current stresses during pre- and post-frontal stages (Roberts et al., 1989; Walker and Hammack, 2000; Draut et al, 2005; Sheremet et al. 2005; Kineke et al., 2006; Jaramillo, 2009; Sheremet et al. 2011). The location and size of the sediment plume (figure 10) is controlled by variations in river discharge and resuspension events, and responds rapidly to varying wind. Southeasterly winds and wind-driven currents force the sediment plume westward and onshore (Moeller et al., 1993; Walker and Hammack, 2000). During the passing of a front, when westerly winds limit the western extent of the plume, the plume broadens to the east and seaward (Moeller et al., 1993; Walker and Hammack, 2000). During post-frontal conditions, strong winds from north or northwest can depress water levels (setdown) in shallow coastal areas (Moeller et. al, 1993; Walker and Hammack, 2000) and can increase resuspension and turbidity levels in the shallow Atchafalaya-Vermillion Bay system by a factor of five (Walker and Hammack, 2000). Subsequently, wind forcing flushes these suspended sediments onto the shelf (Walker and Hammack, 2000), resulting in the sediment plume extending farther offshore.

To investigate a possible correlation of these plume dynamics with the observed differences in modeled and observed wave growth at higher frequencies, satellite images from MODIS Terra 250 were analyzed. The images were obtained from the NASA EOS Data Gateway, processed with HDFLook, and converted from percentage reflectance to an estimate of total suspended matter in the surface layer (Miller and McKee, 2004). Although the concentration estimates are not calibrated with in-situ samples and are

lower than previously reported suspended sediment concentrations (Allison et al., 2000; Kineke et al., 2006), they are useful to identify relative (not absolute) changes in suspended matter.

From the available satellite data (cloud cover limits visibility), the wind-driven plume dynamics was largely as described above (not shown) (Walker and Hammack, 2000). In particular, the westward extent of the plume is pushed farther west during easterly wind conditions, resulting in higher surface sediment concentrations at the experiment site. For example, high sediment concentrations, most likely the result of the high river discharge on March 15, initially are confined mostly to the bay during weak winds from a southerly direction (figure 10a). The plume then extends to the inner shelf (and spreads to the east and west) during strong northerly and northeasterly winds on March 16 (figure 10b). The times when surface suspended sediment concentrations were elevated in the shallow nearshore areas and on the shelf (e.g. March 16 in figure 10b), coincide with the times when the observations show much greater dissipation at higher frequencies (suppression of wave growth) than the model predicts. Although no satellite data are available for the following days (March 17 through 18) when there are significant differences between observed and modeled high-frequency spectral levels with prevailing winds from the east, the plume will be advected farther westward by wind-driven currents that are fairly homogenous throughout the water column (not shown), and surface sediment concentrations at the experiment site will increase further as resettling is hampered by energetic waves (figure 3) and currents. The westward advection of the sediment plume from Atchafalaya Bay into the study area during easterly winds also has been observed during other times, for instance on March 26 when

the observed high-frequency dissipation was greater than predicted by the model (compare figure 7a with figure 7b and figure 7d with figure 7e). When wind-driven currents carry higher surface sediment concentrations westward, wave growth owing to winds appears to be suppressed. In contrast, sediment concentrations are relatively low at the experiment site (e.g. March 8 (not shown), and February 28, figure 10c) when modeled and observed wave evolution are in better agreement, including in the higher-frequency energy balance. Moreover, satellite imagery (not shown) suggests that the location of the western sensor transect often coincides with the maximum western extent of the Atchafalaya sediment plume on the shelf (the plume extends farther westward closer to shore). In addition, the western transect also corresponds to the western most extent of Atchafalaya sediment deposition on the shelf (Draut et al. 2005), possibly explaining the rapid "cleaning" of the surface waters in the study area during westerly winds, and therefore the sensitivity to changes in the wind direction in the model-data comparisons.

Although it is not clear which physical process would relate changes in the surface sediment concentration to the variations in wave growth efficiency and wind-sea dissipation in this area, it is hypothesized that increases in sediment concentration affect the wave energy balance, either through enhanced dissipation of wave energy or by reducing the efficiency of momentum transfer from wind to waves (suppression of growth). The results presented here suggest that the temporal variability of sediment supply by rivers, the local resuspension of sediments by wind, and the subsequent transport in coastal (wind-driven) currents, are important to the evolution of waves propagating across a shallow muddy seafloor.

5 Conclusions

Observations of wave evolution across the Louisiana inner shelf show variability in dissipation rates, which are related to the presence of mud on the seafloor. Comparison of the observations with model hindcasts (SWAN) shows overall good agreement, although observed dissipation rates are somewhat higher than predicted by the model, consistent with earlier findings. During fetch-limited conditions in shallow water, model-data comparisons suggest that wave growth is suppressed by the presence of mud. The observed suppression of wave energy input at higher frequencies (>0.2 Hz) appears to be related to the Atchafalaya plume, which advected mud into the experimental area during easterly winds. These findings suggest that the geographical setting and changes in large-scale meteorological conditions can produce variations in bottom rheology and concentrations of suspended sediment, which affect wave damping and growth characteristics, and thus the coastal wave energy balance.

Acknowledgements

We thank Paul Jessen for the excellent support and data quality control. John Trowbridge, Janet Fredericks, and Greg Stone generously shared their meteorological data. Douglas Alden, Spencer Kawamoto, Paul Harvey, and the crew of R/V PELICAN contributed to the field experiment on the Louisiana shelf, and William Boyd, Levi Gorrell, Erika Ladouceur, and Vera Pavel helped deploy, maintain, and recover the nearshore array. Captain Rodriguez provided the pirate ship Eugenie to guard the nearshore sensors from destruction by trawlers for 50 days in unpleasant sea states. Gail

Kineke provided nearshore bathymetric observations. We thank Arun Chawla for providing WaveWatch III hindcast data. We thank the anonymous reviewers for their helpful and constructive comments and input. This work is supported by the U.S. Office of Naval Research (Littoral Geosciences and Optics Program, and Physical Oceanography Program), the National Oceanographic Partnership Program, the National Science Foundation, and a National Security Science and Engineering Faculty Fellowship.

Appendix

Model implementations

Model hindcasts were made using the third-generation wind-wave model SWAN (version 40.72). SWAN is based on the wave action balance (or radiative transfer equation), which in Cartesian coordinates can be written as (Booij et al., 1999)

$$\frac{\partial}{\partial t}N + \nabla_{\mathbf{x}} \cdot \left(\left[\mathbf{u} + \mathbf{c}_{\mathbf{x}} \right] N \right) + \frac{\partial}{\partial \sigma} c_{\sigma} N + \frac{\partial}{\partial \theta} c_{\theta} N = \frac{S}{\sigma} \qquad (4)$$

where $N = N(\sigma, \theta)$ is the action density defined as energy density over (relative) frequency, $\mathbf{x} = (x, y)$ are the coordinates of the physical space, and (σ, θ) are the (relative) frequency and direction coordinates of the spectral space. The $\mathbf{c_x}$, c_σ, and c_θ are the propagation speed of the action density in the spatial domain, in frequency space, and in directional space, respectively. On the right side of equation (5) the source term $S = S(\sigma, \theta)$ represents the combined effects of generation (wind), dissipation (bottom friction, white capping, depth-induced wave breaking), and non-linear wave-wave interactions (triads and quadruplets). Other dissipation processes (e.g. vegetation damping) are available in SWAN (see SWAN implementation manual, available at http://www.swan.tudelft.nl), but were not used in this study.

Grids and Physics

Simulations were performed on a 2D, regular rectangular computational grid, covering an area of ~ 59 x 34 km (see figure A1 and table A1 for further information).

The model was run in non-stationary mode, with hourly updated wave, wind, and water level variations. Wave boundary conditions for the southern boundary (see figure A1) were taken from frequency-directional spectra estimated from observations at stations dw12 and pv16, projected onto the boundary along a line of constant latitude. The observed wave conditions were linearly interpolated along the boundary.

Side-boundaries for the domain were updated using 1D non-stationary runs (along the boundary) to prevent the occurrence of spurious shadow zones and energy leakage.

The model was run in third-generation mode (GEN 3) with saturation-based whitecapping (Van der Westhuysen et al., 2007) and a slight modification of the Yan wind formulation (Yan, 1987) as proposed by Van der Westhuysen et al., (2007). For comparison, simulations were conducted with Komen et al. (1984) physics with a wavenumber-dependent whitecapping formulation (Rogers et al., 2003), which gave similar results. All available source terms were included in the computations except the triad interactions.

Bottom friction

One of the objectives of the hindcast study is to identify the differences in the wave evolution observed over a muddy seafloor relative to that anticipated over a sandy shelf. Therefore, a specific mud model was not implemented (Dalrymple & Liu, 1978; Winterwerp et al., 2007; Rogers & Holland, 2009), but instead a standard bottom friction term (Hasselmann et al., 1973) with a fixed bottom friction coefficient (0.038 m^2s^{-3}) was used to account for frictional losses of wave energy that would be present over a sandy shelf. Although the observations include low-frequency swell, wind-sea, and mixed events for which different bottom friction coefficients often are used (Bouws and Komen,

1983), recent studies (Van Vledder et al. 2010; Zijlema et al., 2012) suggest the use of a single, fixed JONSWAP bottom friction coefficient of 0.038 m^2s^{-3}, independent of the frequency range of the waves (sea or swell).

Winds and currents

Wind forcing was obtained from hourly averaged meteorological observations made in 6-m water depth near the western transect (figure 1b), corrected for winds at 10 m (Johnson, 1999, and references therein). To account for the down-wind variability of the atmospheric boundary layer owing to the decrease in roughness length over water, wind speeds during offshore wind events (defined as wind events with mean wind directions $< \pm \frac{\pi}{2}$ from exactly offshore) were modified by a spatially varying scaling factor (Taylor & Lee, 1984).

The wind input is critical for meaningful comparisons, and thus simulations were run with winds from the National Centers for Environmental Prediction (NCEP) Global Forecast System (GFS) analysis, which provides three-hourly wind information on a 4-minute grid. The scaled wind field compares well with the NCEP -winds (figure A2). Model results with the NCEP winds also were similar to the simulations with the observed (and scaled) winds with only minor (and non-systematic) differences.

Comparison of observed currents between the four ADPs in the array (pv2, pv4, pv7, pv9) showed little difference over the experimental period, so for the simulations the flow field was assumed to be homogeneous. The flow field used in the simulations was taken from the ADP at station pv4. Simulations without currents showed similar results and omission, of the current field would not have altered the conclusions.

Bathymetry and water level variations

Bathymetry was taken from the NOS coastal relief model, augmented with nearshore observations made during the experiment. Water level variations, mostly owing to tidal changes (maximum amplitude ~ 60 cm), were obtained from the observations by taking the mean (over all sensors) of the difference between the hourly-averaged, observed water depths, and the local water depth from the bathymetry data.

References

Allison, M., Kineke, G., Gordon, E., Goñi, M., 2000. Development and reworking of a seasonal flood deposit on the inner continental shelf off the Atchafalaya River. Continental Shelf Research. 20, 2267–2294.

Ardhuin, F., T. H. C. Herbers, G. P. van Vledder, K. P. Watts, R. Jensen, H. C. Graber ,2007. Swell and slanting-fetch effects on wind wave growth, Journal of Physical Oceanography, 37, 908–931, doi:10.1175/JPO3039.1.

Booij, N., Ris, R.C., Holthuijsen, L.H., 1999. A third-generation wave model for coastal regions. 1. Model description and validation. Journal of Geophysical Research, 104(C4), 7469-7666.

Bouws, E., Komen, G.J., 1983. On the balance between growth and dissipation in an extreme, depth limited wind-sea in the southern North Sea, Journal of Physical Oceanography, 13, 1653-1658.

Dalrymple, R.A., Liu, P. L.-F., 1978. Waves Over Soft Muds: A Two-Layer Fluid Model. Journal of Physical Oceanography, 8, 1121-1131.

Draut, A.E., Kineke, G. C., Huh O.K., Grymes J.M. I., Westphal K.A., 2005. Coastal mudflat accretion under energetic conditions, Louisiana chenier-plain coast, USA. Marine Geology, 214, 27– 47.

Draut, A., Kineke, G., Velasco, D., Allison, M., Prime R., 2005. Influence of the Atchafalaya River on recent evolution of the chenier-plain inner continental shelf, northern Gulf of Mexico. Continental Shelf Research, 25, 91–112.

Elgar, S., Raubenheimer, B., 2008. Wave dissipation by muddy seafloors. Geophysical Research Letters, 35, L07611, doi:10.1029/2008GL033245.

Engelstad, A., 2011. Damping characteristics of wave propagation across the muddy Louisiana shelf. MSc dissertation, San Francisco State University, San Francisco 60p.

Gade, H.G., 1958. Effects of a non-rigid, impermeable bottom on plane surface waves in shallow water. Journal of Marine Research 156 (2), 61–82.

Garcia-Garcia, A., Janssen, T.T., Herbers, T.H.C., Alden, D., Orange, A., Orange, D., Jessen, P., Kawamoto, S., Harvey, P., 2011. A geophysical baseline for the Fluid-Mud MURI site, west of

Atchafalaya Bay. Under review at Geo-Marine Letters.

Jaramillo, S., Sheremet, A., Allison, M.A., Reed, A.H., Holland, K.T., 2009. Wave‐mud interactions over the muddy Atchafalaya subaqueous clinoform, Louisiana, United States: Wave‐supported sediment transport. Journal of Geophysical Research, 114, C04002, doi:10.1029/2008JC004821.

Johnson, H.K. 1999. Simple expressions for correcting wind speed data for elevation. Coastal Engineering, 36 (3), 263-269, ISSN 0378-3839, doi: 10.1016/S0.

Kineke, G.C., Higgins E.E., Hart, K., Velasco D., 2006. Fine-sediment transport associated with cold-front passages on the shallow shelf, Gulf of Mexico, Continental Shelf Research, 26 (17–18), 2073-2091.

Komen, G.J., Hasselmann, S., Hasselmann, K., 1984. On the existence of a fully developed wind-sea spectrum, Journal of Physical Oceanography, 14, 1271– 1285.

MacPherson H., 1980. The attenuation of water waves over a non-rigid bed. Journal of Fluid Mechanics, 97, pp 721-742 doi:10.1017/S0022112080002777

Mei, C.C., Liu, K.-F., 1987. A Bingham-plastic model for a muddy seabed under long waves. Journal of Geophysical Research, 92, 14581–14594.

Miller, R.L., and B.A. McKee (2004), Using MODIS Terra 250 m imagery to map concentrations of suspended matter in coastal waters, Remote Sens. Environ., 93, 259–266.

Moeller, C. C., Huh, O.K., Roberts, H.H., Gumley, L.E., Menzel, W.P., 1993. Response of Louisiana coastal environments to a cold-front passage. Journal of Coastal Research, 9(2), 434-447.

Ng, C.O., 2000. Water waves over a muddy bed: a two-layer Stokes' boundary layer model. Coastal Engineering 40 (3), 221–242.

Piedra Cueva, I., 1993. Mass transport in mud layer induced by wave action. Proc. Natl. Conf. Hydraul. Eng., ASCE, 1189–1193.

Roberts, H.H., Huh, O.K., Hsu, S.A., Rouse Jr., L.J., Rickman, D.A., 1989. Winter storm impacts on the chenier plain coast of southwestern Louisiana. Transactions—Gulf Coast Association of Geological Societies 39, 515–522.

Rogers, W.E., Holland, T., 2009. A study of dissipation of wind-waves by mud at Cassino Beach, Brazil: prediction and inversion. Journal of Coastal Research, 29, 676-690.

Rogers, W.E., Hwang, P.A., Wang, D.W., 2003. Investigation of wave growth and decay in the SWAN model: Three regional-scale applications. Journal of Physical Oceanography 33, 366–389.

Sheremet, A., Jaramillo, S., Su, S.-F., Allison, M.A., Holland, K.T., 2011. Wave-mud interaction over the muddy Atchafalaya subaqueous clinoform, Louisiana, United States: Wave processes. Journal of Geophysical Research, 116, C06005, doi:10.1029/2010JC006644.

Sheremet, A., Mehta, A.J., Liu, B., Stone, G.W. 2005. Wave–sediment interaction on a muddy inner shelf during Hurricane Claudette. Estuarine, Coastal and Shelf Science, 63(1-2), 225–233.

Sheremet, A., Stone, G.W., 2003. Observations of nearshore wave dissipation over muddy sea beds. Journal of Geophysical Research, 108(C11), 3357.

Taylor, P.A., Lee, R. J., 1984. Simple guidelines for wind speed variations due to small-scale topographic features. Climatological Bulletin, 18, 3-32.

Trainor, L.T., 2009. Field observations and SWAN model predictions of wave evolution in a muddy coastal environment. MSc dissertation, Naval Postgraduate School, Monterey 73p.

Van der Westhuysen, A.J., Zijlema, M., Battjes, J.A., 2007. Nonlinear saturation-based whitecapping dissipation in SWAN for deep and shallow water. Coastal Engineering 54 (2), 151–170.

Van Vledder, G., Zijlema, M., Holthuijsen, L., 2010. Revisiting the JONSWAP bottom friction formulation. Proceedings Of The 32nd International Conference On Coastal Engineering, 1(32).

Walker, N.D., Hammack, A.B., 2000. Impacts of winter storms on circulation and sediment transport: Atchafalaya-Vermilion Bay Region,Louisiana,U .S.A. Journal of Coastal Research,1 6(4), 996-1010.

Wells, J.T., Kemp, G.P., 1981. Atchafalaya mud stream and recent mudflat progradation: Louisiana chenier plain. Transactions—Gulf Coast Association of Geological Societies 31, 39–46.

Winterwerp, J.C., de Graaff, R.F., Groeneweg, J., Luyendijk, A.P., 2007. Modelling of wave damping at Guyana mud coast. Coastal Engineering 54, 249–261.

Yan, L., 1987. An improved wind input source term for third generation ocean wave modelling, Scientific report WR-No 87-8, De Bilt, The Netherlands.

Zijlema M., van Vledder G.Ph., Holthuijsen L.H., 2012. Bottom friction and wind drag for wave models, Coastal Engineering 65, 19-26.

Figure Captions

Figure 1. (a) The study area is located west of the Atchafalaya-Vermillion Bay system in the Gulf of Mexico. (b) Bathymetry (black curves are isobaths, units m) and sensor locations. Blue dots are the inner shelf stations where dw-stations are Datawell Directional Waverider buoys, the pv are Nortek Vector ADV-pressure sensors, and pa are pressure sensors. The nearshore array of SONTEK Triton ADV-pressure sensors (referenced in the text as n1, n2, …., n16), is indicated with red squares. The green triangle shows the location of the meteorological buoy.

Figure 2. (a) Wind speed and (b) wind direction (black curves) and mean wave direction (blue) at station pv2 in 11.3 m water depth versus time. Directions are defined as where the waves and wind are from. (c) Peak periods on the western transect in 11.3 m (pv2, red) and 1.7 m (n4, black) water depth. (d) Significant wave height in 11.3 m (pv2, red) and 1.7 m (n4, black) water depth. The black dashed line in (c) at 6 sec and in (d) at 1 m are for reference. The data gap between March 2 and March 5 is during instrument maintenance. Shaded areas refer to events discussed in the text and indicate periods with large spatial wave variability and strong (> 9 m/s) winds from the northeast (yellow, 0 < dir < 80 deg) and northwest (gray, 300 < dir < 360 deg), as well as a period of large swell (blue).

Figure 3. Significant wave height versus time across (a) the western transect in 11.3- (pv2, red curve), 8.3- (pv4, black), 3.9- (n15, blue), and 1.7-m (n4, green) water depths, (b) the central transect in 10.9- (pv7, red) and 8.3-m (pv9, black) water depths, and (c) the eastern transect in 10.9- (dw12, red) and 5.5-m (pv16, black) water depths. The dashed black lines at 1m height are for reference. Data gaps for shelf stations between March 2 and March 5 are due to instrument maintenance. Shaded areas refer to events discussed in the text and indicate periods with large spatial wave variability and strong (> 9 m/s) winds from the northeast (yellow, 0 < dir < 80 deg) and northwest (gray, 300 < dir < 360 deg), as well as a period of large swell (blue).

Figure 4. Observed (red curves with dots) and modeled (black curves with triangles) significant wave height along the western transect versus time in (a) 11.3, (b) 8.3, (c) 3.9, and (d) 1.7 m depth. The data gaps (panels a, and b) between March 2 and March 5 are during instrument maintenance.

Figure 5. Modeled versus observed significant wave height for all stations on the western and central transects for (a) onshore winds (130°-250° true north) and (b) offshore winds (310° -70°). (Cross-shore is rotated 10^o clockwise from true north). The dashed black lines indicate perfect agreement. The slope of the best-fit line is 0.94 for (a) and 1.18 for (b), $r^2 = 0.94$ for (a) and $r^2 = 0.71$ for (b), and the root mean square error is 0.11 m for (a) and 0.19 m for (b).

Figure 6. Observed (red curves with circles) and modeled (black curves with triangles) variance densities (top panels) and wave directions (bottom panels) versus frequency for stations in (a and e) 1.7, (b and f) 3.9, (c and g) 8.3, and (d and h) 11.3 m depth in the afternoon of February 26. Wave direction is defined as where the waves come from.

Figure 7. Contours (color scales on the right) of (a and d) observed energy flux gradients, (b and e) modeled (SWAN) energy flux gradients, and (c and f) observed energy density as a function of frequency and time. a-c are between 11.3 and 8.9 m depth and d-f are between 3.9 and 2.5 m depth. Positive flux gradients indicate generation, negative flux gradients indicate dissipation. Note the different scales of (a) and (b) versus (d) and (e).

Figure 8. Modeled versus observed integrated growth rates between 11.3 m (pv2) and 8.3 m (pv4). Integration limits are (a) 0.04-0.20 Hz and (b) 0.20-0.25 Hz. Positive (negative) values indicate growth (dissipation) rates. Note different vertical and horizontal scales in (a) versus (b). Red circles indicate times with wind coming from between 30° and 130° true north and black triangles are for all other directions. Cross-shore is rotated about 10^o clockwise from true north. Only events for which $H_s \geq 0.5$ m at pv2 are shown. The dashed black lines indicate perfect agreement.

Figure 9. Observed (red circles) and modeled (black triangles) growth rates (right-hand axis) and wind (grey curve) and current (green dashed curve) directions (left-hand axis) versus time. Only events for which $H_s \geq 0.5$ m at pv2 are shown.

Figure 10. Estimate of total suspended-matter concentrations (from Modis 250 imagery) on (a) March 15, (b) March 16, and (c) February 28. All images were recorded around 17:00 o'clock GMT. High concentrations are red, low concentrations are blue (color scale on right). Grey shading is land. Instrument locations are shown with black circles (shelf stations) and red squares (shoreward stations).

Figure A1. Boundary conditions for the southern boundary (red line) were taken from observations (dw12 and pv16). 1D non-stationary runs, initiated by dw12 and pv16 for the western and eastern boundary (blue lines), respectively, were used as side-boundaries.

Figure A2. Wind speed for (a) shoreward and (b) seaward stations (the southern computational boundary), and (c) direction versus time. NCEP wind data (blue curves with triangles) and scaled winds from observations in ~6 m water depth (black curves with dots) are shown for the experimental period. Wind directions (c) for NCEP wind data are shown seaward, whereas the observations (black curves with dots) are assumed homogenous and are therefore left unchanged.

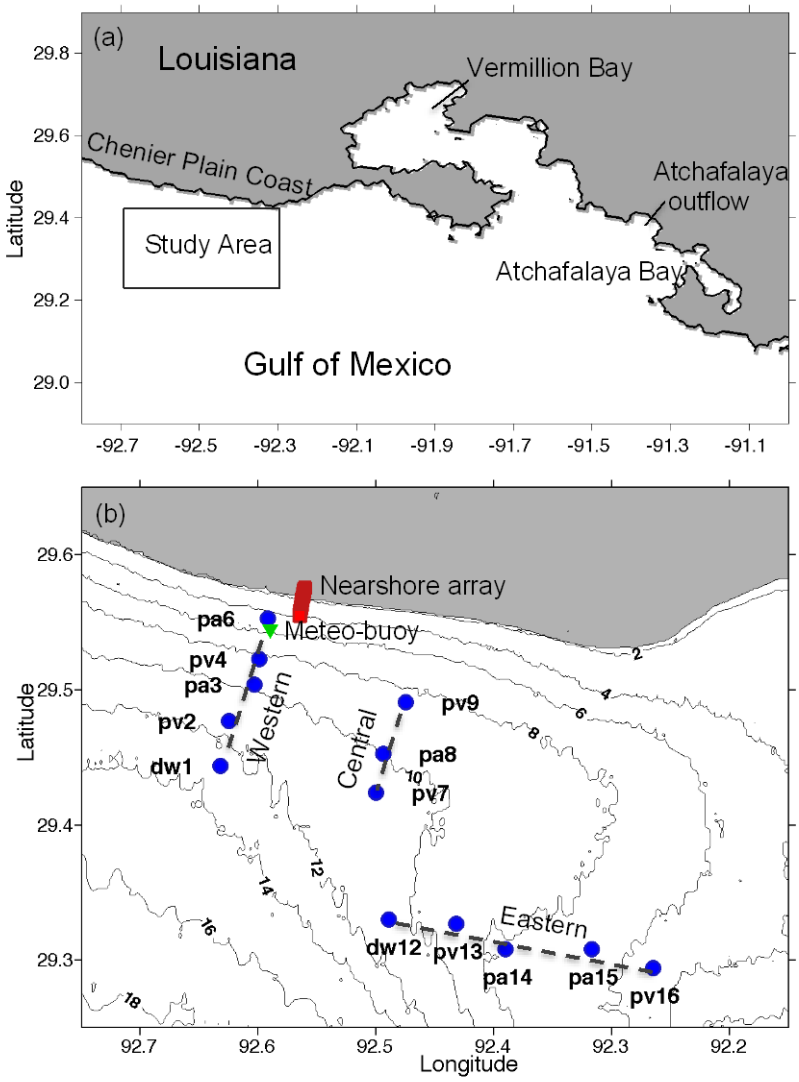
(a)
Louisiana
Vermillion Bay
Chenier Plain Coast
Atchafalaya outflow
Study Area
Atchafalaya Bay
Gulf of Mexico
Latitude
29.8
29.6
29.4
29.2
29.0
-92.7
-92.5
-92.3
-92.1
-91.9
-91.7
-91.5
-91.3
-91.1
(b)
Nearshore array
Meteo-buoy
pa6
pv4
pa3
pv2
dw1
pv9
pa8
pv7
dw12
pv13
pa14
pa15
pv16
Western
Central
Eastern
2
4
6
8
10
12
14
16
18
Latitude
29.6
29.5
29.4
29.3
92.7
92.6
92.5
92.4
92.3
92.2
Longitude

Figure 1

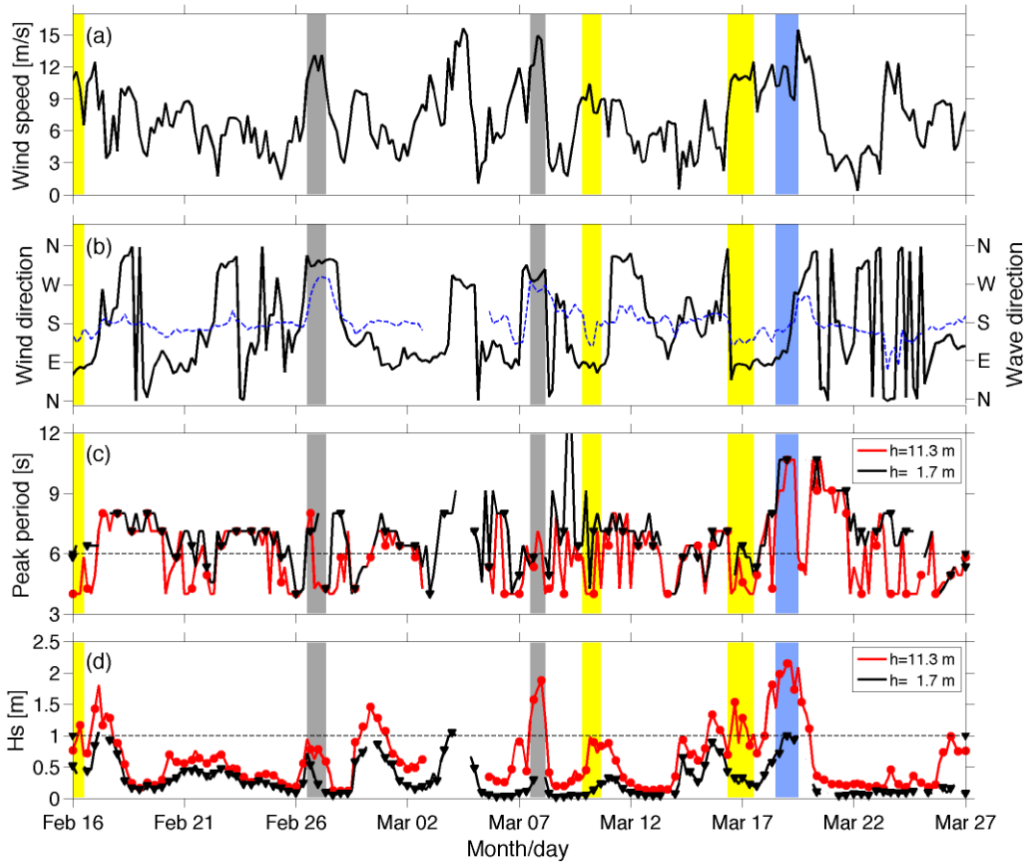

Figure 2

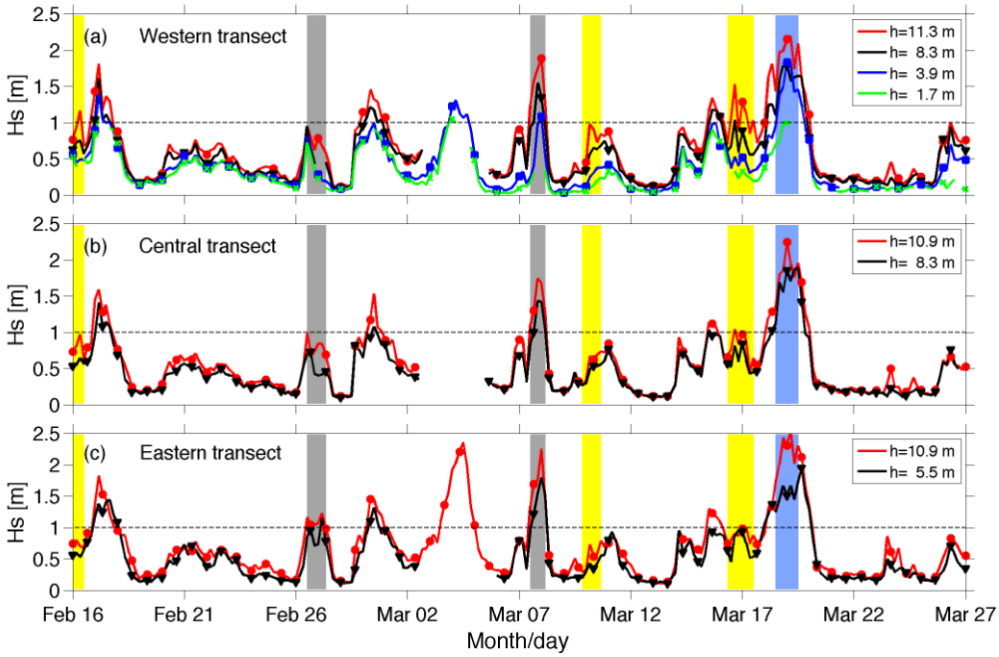

Figure 3

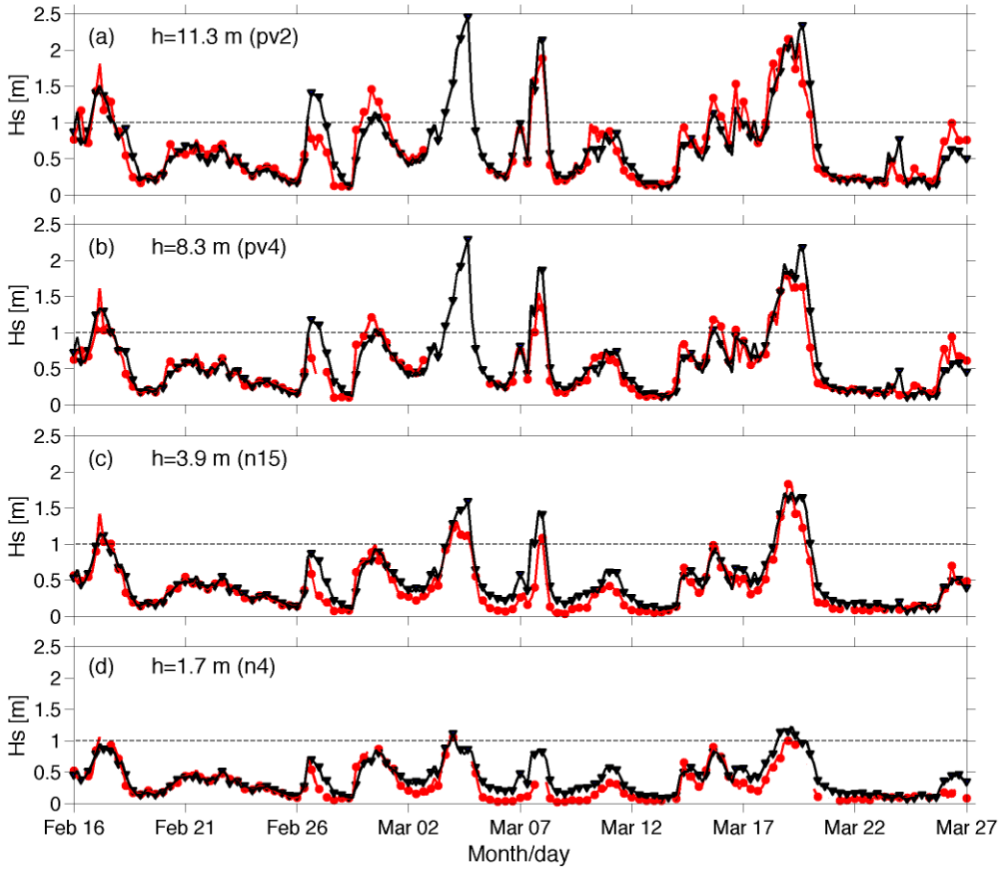

Figure 4

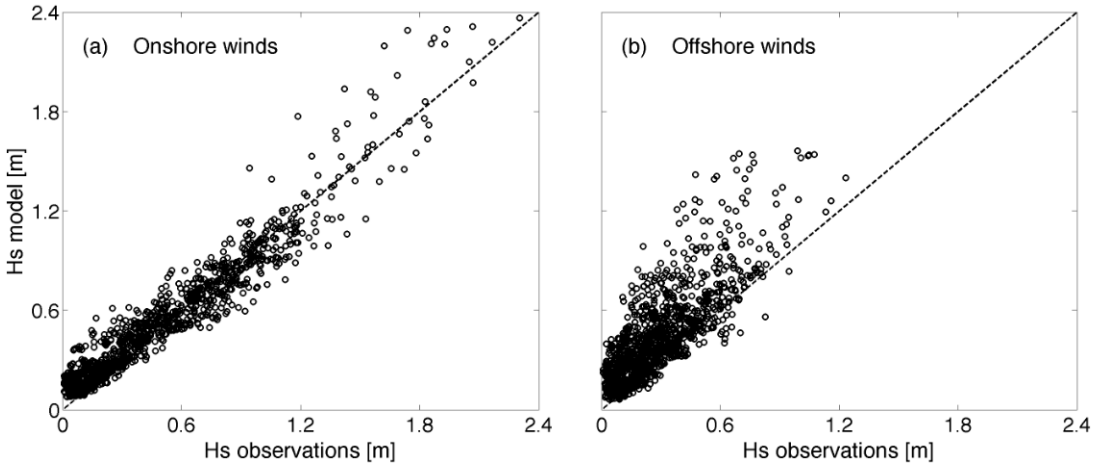

Figure 5

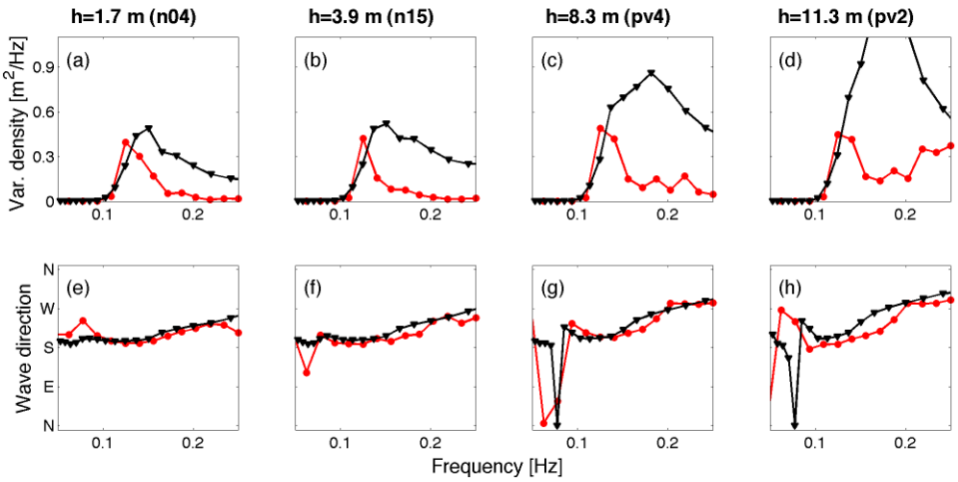
h=1.7 m (n04)
h=3.9 m (n15)
h=8.3 m (pv4)
h=11.3 m (pv2)
(a)
(b)
(c)
(d)
(e)
(f)
(g)
(h)
Var. density [m²/Hz]
0.9
0.6
0.3
0
Wave direction
N
W
S
E
N
0.1
0.2
Frequency [Hz]

Figure 6

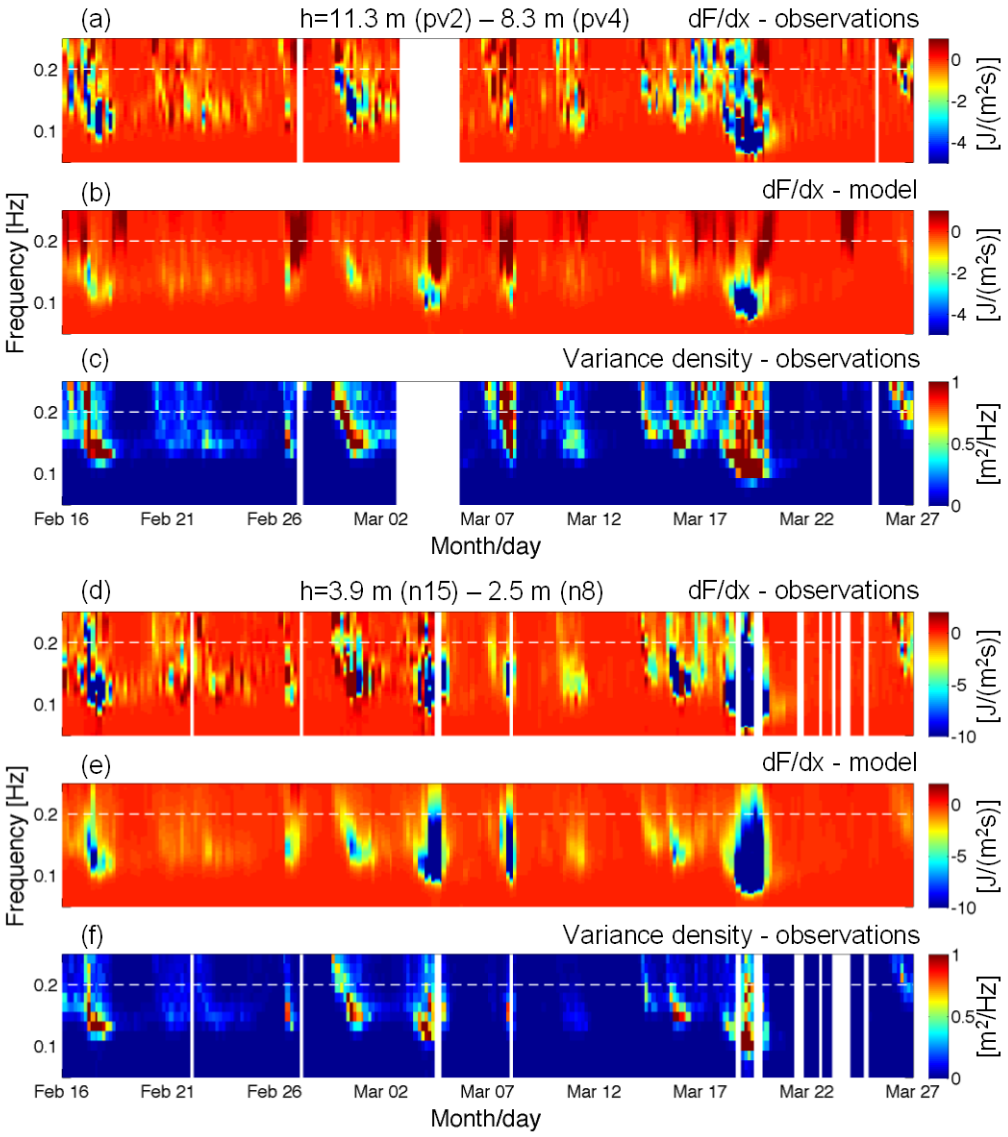
(a)
h=11.3 m (pv2) – 8.3 m (pv4)
dF/dx - observations
(b)
dF/dx - model
(c)
Variance density - observations
(d)
h=3.9 m (n15) – 2.5 m (n8)
dF/dx - observations
(e)
dF/dx - model
(f)
Variance density - observations
Frequency [Hz]
0.2
0.1
[J/(m²s)]
[m²/Hz]
Feb 16
Feb 21
Feb 26
Mar 02
Mar 07
Mar 12
Mar 17
Mar 22
Mar 27
Month/day

Figure 7

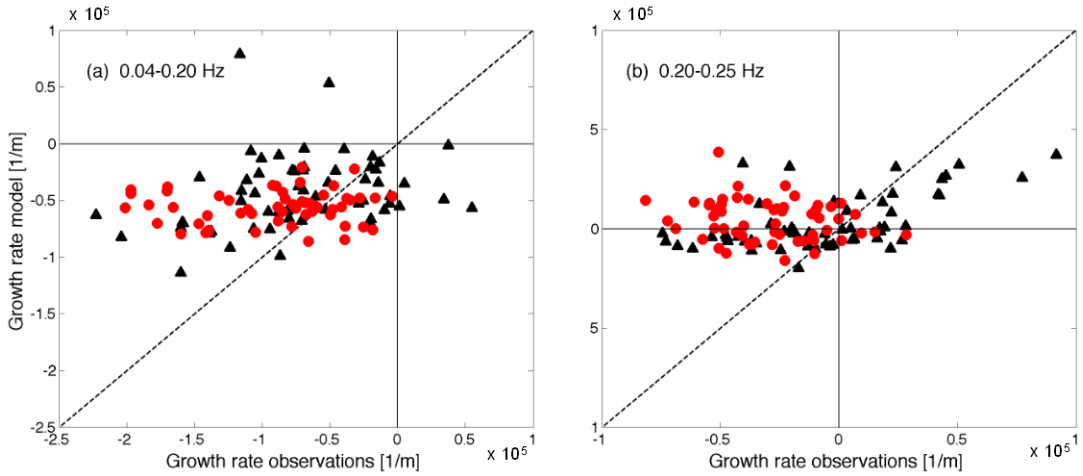

Figure 8

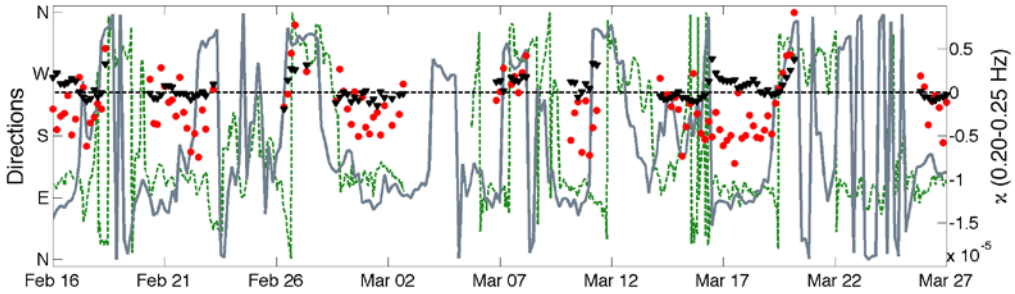

Figure 9

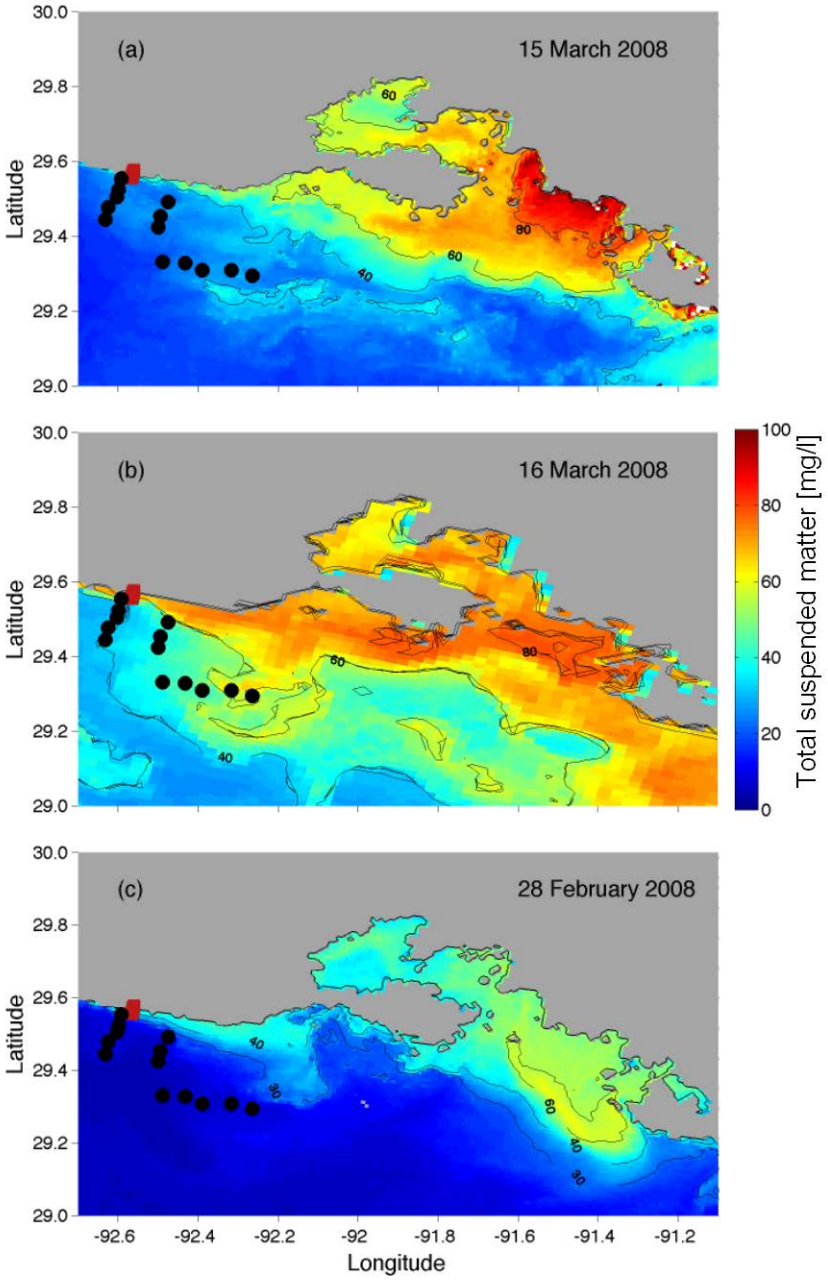
(a)
15 March 2008
(b)
16 March 2008
(c)
28 February 2008
Latitude
Longitude
30.0
29.8
29.6
29.4
29.2
29.0
-92.6
-92.4
-92.2
-92
-91.8
-91.6
-91.4
-91.2
Total suspended matter [mg/l]
100
80
60
40
20
0

Figure 10

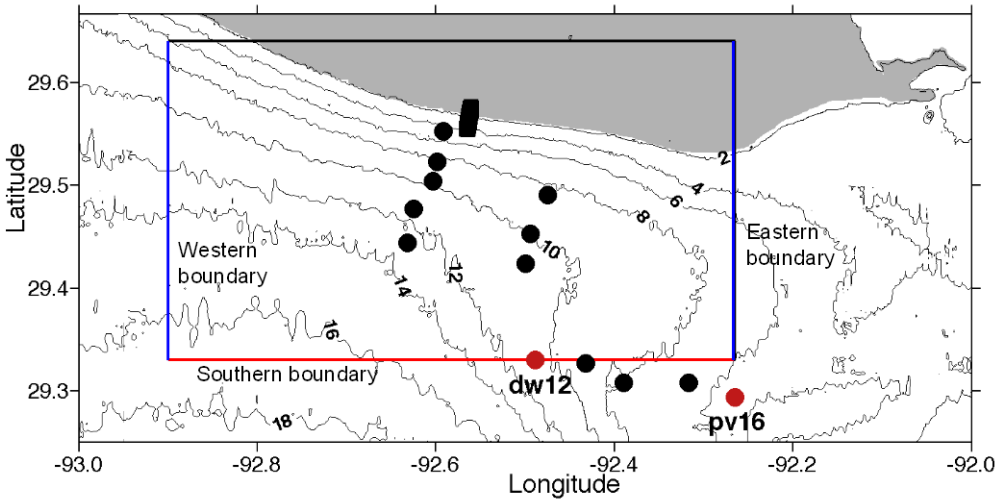

Figure A1

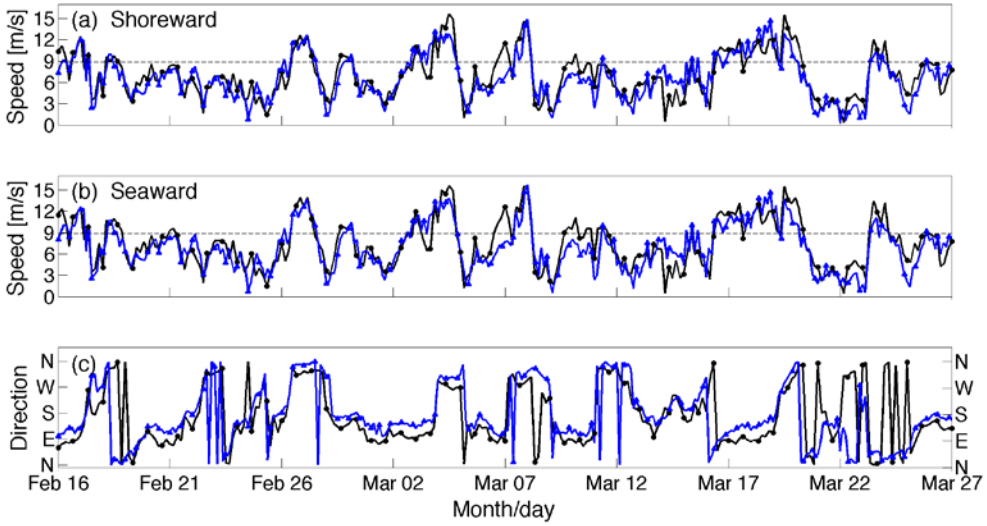

Figure A2

Tables

Western transect, shelf				
Station name	Latitude (Deg. North)	Longitude (Deg. West)	Depth (MSL) (m)	Notes
dw1	29.44418	92.63243	13.3	available only until 03/05/2008
pv2	29.47670	92.62452	11.3	
pa3	29.50370	92.60323	9.6	
pv4	29.52315	92.59897	8.3	ADP used for 1st leg
pa6	29.55330	92.59190	4.6	misplaced by fisher boat, but depth still ok
Western transect, nearshore				
Station name				
n16	29.55618	92.56444	4.0	
n15	29.55764	92.5640	3.9	
n14	29.55896	92.56389	3.7	
n13	29.56041	92.56358	3.6	
n12	29.5617	92.56331	3.4	
n11	29.56311	92.56314	3.2	
n9	29.56446	92.56289	2.8	
n8	29.5660	92.56245	2.5	

n7	29.56851	92.56195	2.2	
n6	29.56999	92.56165	2.0	
n5	29.57142	92.56120	1.9	
n4	29.57273	92.56110	1.7	
n3	29.57413	92.56084	1.4	
n2	29.57543	92.56051	1.3	

Central transect				
Station name				
pv7	29.42407	92.49975	10.9	
pa8	29.45290	92.49433	9.9	
pv9	29.49110	92.47482	8.3	
Eastern transect				
Station name				
dw12	29.32995	92.48897	10.9	
pv13	29.32675	92.43167	8.8	
pa14	29.30833	92.38973	7.6	
pa15	29.30785	92.31747	6.8	
pv16	29.29388	92.26530	5.5	

Table 1. Station information for sensors: dw are Datawell Waverider buoys, pv are shelf pressure-velocity sensors, pa are pressure recorders; the n* represent colocated pressure and velocity sensors in the nearshore. Heights above the seafloor of the bottom-mounted instruments were 1.35 m for the ADPs, 1.5 m for the pressure-velocity sensors, and 0.7 m for the pressure recorders. The nearshore pressure sensors and ADVs were located 0.6 m and 0.9 m above the bottom, respectively.

	1D	2D
Mode	**Non-stationary**	**Non-stationary**
Computational grid (spherical)	1 x 125 (N-S)	175 (E-W) x 125 (N-S)
Computational resolution	0.0036° x 0.0025° (~338.1 m x 272.8 m)	0.0036° x 0.0025° (~338.1 m x 272.8 m)
Discrete frequency range	0.04-1.0 Hz	0.04-1.0 Hz
Bottom grid	1 x 500 (N-S)	1200 (E-W) x 500 (N-S)
Bottom resolution	0.000833° x 0.000833° (~72.5 m x 91.6 m)	0.000833° x 0.000833° (~72.5 m x 91.6 m)
Directional resolution	10°	10°
Iterations (average)	4	6
Time steps	10 minutes. Wave, wind, and water level variations updated every hour.	10 minutes. Wave, wind, and water level variations updated every hour.
Physics	Wind generation, Yan White-capping, Westhuysen Depth induced wave breaking (gamma = 0.73) Bottom friction (JONSWAP = 0.038 m^2s^{-3}) Quadruplets (DIA)	Wind generation, Yan White-capping, Westhuysen Depth induced wave breaking (gamma = 0.73) Bottom friction (JONSWAP = 0.038 m^2s^{-3}) Quadruplets (DIA)
Boundaries	Eastern boundary initiated by pv16 (updated every 4 hrs). Western boundary initiated by dw12 (updated hourly).	Southern boundary initiated by dw12 (updated hourly) and pv16 (updated every 4 hrs). Eastern boundary conditions from 1D runs Western boundary conditions from 1D runs.
Propagation scheme	BSBT	BSBT

Table A1. Implementations for 1D and 2D non-stationary SWAN runs.